CuO/SBA-15 materials synthesized by solid state grinding: Influence of CuO dispersion and multicycle operation on DeSO$_X$ performances

Pierrick Gaudin [a], Sophie Dorge [b], Habiba Nouali [a], Matthieu Vierling [c], Emmanuel Fiani [d], Michel Molière [e], Jean-François Brilhac [b], Joël Patarin [a,*]

[a] Equipe Matériaux à Porosité Contrôlée, Institut de Science des Matériaux de Mulhouse, UMR CNRS 7361, Université de Haute Alsace, 3 bis rue Alfred Werner, 68093 Mulhouse Cedex, France
[b] Laboratoire de Gestion des Risques et Environnement, Université de Haute Alsace, 3 bis, rue Alfred Werner, 68093 Mulhouse Cedex, France
[c] GE Energy, 20 avenue du Maréchal Juin, 90007 Belfort Cedex, France
[d] Agence de l'Environnement et de la Maîtrise de l'Energie, 20 avenue du Grésillé, BP 90406, 49004 Angers Cedex 01, France
[e] Université de Technologie de Belfort-Montbéliard, 90010 Belfort Cedex, France

ARTICLE INFO

ABSTRACT

In this study, copper oxide (CuO) has been dispersed into an organized mesoporous silica (SBA-15) using the solid state grinding method. The resulting CuO/SBA-15 materials were evaluated as SO$_x$ adsorbents and were fully characterized before and after sulfation. The influence of the calcination conditions on the copper dispersion was studied. Results show that the textural properties of the materials and the formed copper species are closely related to the calcination procedure. The adsorption performances increase with the copper dispersion. It was found that despite the high GHSV value used in this work (25,000 h^{-1}), the highly dispersed copper species confer a high efficiency to the adsorbent. Cyclic adsorption/regeneration experiments show a surprising but explainable increase in the adsorption efficiency in the second cycle followed by a slight but monotonic deactivation in the subsequent cycles, as a result of the progressive sintering of the copper species.

© 2015 Elsevier B.V. All rights reserved.

1. Introduction

Among the pollutants resulting from human activity, SO$_X$ (e.g., SO$_2$ + SO$_3$) are recognized as very harmful to human health and to the environment due to their role in the formation of acid rains and secondary aerosols in the atmosphere [1]. In order to minimize such effects, national emission ceilings have been set, inter alia, for SOx emissions at the international level through the Gothenburg Protocol and at the European level through the NEC (National Emission Ceilings) Directive 2001/81/EC. SO$_X$ emissions mainly originate from the combustion of fossils fuels, e.g., power generation plants. Consequently, SO$_x$ emissions from stationary sources are strictly regulated through the IED (Industrial Emissions Directive) 2010/75/EU, with the obligation to achieve significant reduction rates by using appropriate SOx abatement technologies such as flue gas desulfurization (FGD) or to switch to low sulfur fuels. Regarding conventional FGD, desulfurization processes are generally based on two approaches: dry sorption or wet scrubbing [2,3] which both use non regenerable alkaline or alkaline-earth compounds. Although the efficiency of these processes is well established, they still suffer from major drawbacks among which their high energy consumption and the production of large amounts of solid and/or liquid wastes (sodium or calcium sulfate). Therefore, there is the need for alternative processes in which, for instance, SO$_x$ will be reversibly adsorbed on regenerable solids. Such adsorbents must be bi-functional as they must be able to:

Catalyze the oxidation of SO$_2$ to SO$_3$: $SO_2 + \frac{1}{2}O_2 \rightarrow SO_3$

Chemisorb SO$_3$ as metallic sulfate : $xSO_3 + MO_x \rightarrow M(SO_4)_x$

Another important requirement is the potential of regeneration along multicycle operation while retaining an optimum SO$_x$ storage capacity. The regeneration of the adsorbent is usually performed by thermal decomposition of the sulfate:

$M(SO_4)_x \rightarrow xSO_3 + MO_x$

The SO$_3$ generated during this regeneration step can then be used to produce marketable H$_2$SO$_4$ or elementary sulfur [3].

* Corresponding author. Fax:: +33 3 89 33 68 85.
E-mail address: joel.patarin@uha.fr (J. Patarin).

During the last decades, the capture of SO_X has been the subject of numerous studies and a large variety of materials such as CaO, MgO, TiO_2, MnO_2, CeO_2, Al_2O_3, oxides supported on Al_2O_3 or on carbonaceous materials, zeolites, clays, mixed oxides etc. were evaluated as potential adsorbents for capturing SO_X [2]. The nature and composition of the adsorbent depend on the experimental conditions and more especially on the temperature involved in the process. Copper oxide supported on alumina has been reported as a promising material for SO_X chemisorption between 300 and 500 °C [3–9], which is a suitable temperature window for boiler or gas turbine combined cycle applications. Indeed, in this temperature range, CuO exhibits a good activity both for the catalytic oxidation of SO_2 to SO_3, and for the chemisorption of SO_3 as $CuSO_4$. Moreover, the decomposition temperature of $CuSO_4$ is relatively low (lower than 700 °C) which allows to regenerate the adsorbent while both limiting the consumption of heat and preventing the thermal degradation of the support. For this reason, alumina supported copper oxide has been the subject of extensive evaluation [3–9]. However, a drawback of CuO/Al_2O_3 based adsorbents lies in the limited specific surface area of alumina as compared with that of mesoporous silica. Moreover, the alumina support itself undergoes sulfation [4,6,10], which entails a loss of its textural properties, resulting in the decrease of the adsorbent lifetime, especially if it undergoes deep sulfation [3]. On the contrary, mesoporous SiO_2 supports boast the highest surface area properties and are inert with respect to SO_X [11].

Given that the bulk sulfation of CuO particles suffers from strong kinetic limitations due to the slow diffusion of SOx [4], the aim of the present study was to develop highly dispersed SiO_2-supported CuO materials to obtain an optimal sulfation efficiency. Organic Mesoporous Silica (OMS) such as SBAs, MCMs or KIT-6 have attracted attention of researchers since their particularly high specific surface areas and porous volumes make them ideal for the incorporation of different species, including metal oxides [12–14] and especially copper oxide [15–23]. The pore size of SBA-15 that lies in the range of 5–10 nm is expected to enable a good diffusion of gaseous species through the mesoporous network. For these reasons, SBA-15 was chosen as paradigmatic OMS-type support for CuO based SOx adsorbents.

It is well known that the degree of dispersion of metal oxide on a support obtained through an impregnation step is closely related to a number of parameters among which the most important are: the nature of the support [24,25], the metal precursor [25,26], the solvent used [27], the drying step [28,29], the calcination conditions [24,30–39] and especially the impregnation method [24,25,29,40]. Particularly, the growth of metal oxide particles during the decomposition step of the metal precursor can result in the plugging of the pores [33,36,40,41] and/or in a migration of metal oxide outside the porous structure [36,38,40]. Wang et al. reported an original impregnation method [42] consisting in grinding the as-synthesized SBA-15 material (still containing the surfactant in the porous network) with the copper precursor. Besides its simplicity and the fact that only one calcination step allows at the same time the removal of the organic template and the decomposition of the metal precursor, this method was reported to yield highly dispersed copper species in the mesoporous channels of the support [43–48]. For these reasons, such a method was used in the present work with a special emphasis on the influence of the calcination conditions. The materials obtained were investigated as adsorbents for SO_X chemisorption and were extensively characterized before and after sulfation, using: nitrogen physisorption, X-Ray diffraction (XRD), X-Ray fluorescence (XRF), scanning (SEM) and transmission electron microscopy (TEM). The SO_x chemisorption capacity of the adsorbents was determined using a fixed bed reactor device.

2. Experimental section

2.1. Synthesis of SBA-15 mesoporous silica

The SBA-15 mesoporous silica was synthesized as follows: 10.5 g of Pluronic 123 (Sigma–Aldrich) were dissolved in a solution containing 50 mL of HCl (37%, Sigma–Aldrich) and 330 mL of distilled water, at 55 °C in a 500 mL beaker. After complete dissolution, 22.5 g of tetraethylorthosilicate (Sigma–Aldrich) were added and the solution was kept under stirring for 24 h at 55 °C. The temperature was then raised up to 90 °C for 24 h. The precipitate obtained was filtered, washed with distilled water and dried at 90 °C overnight. This material, still containing the Pluronic 123 surfactant in the mesoporous network is denoted as "as-synthesized SBA-15" (As-SBA-15). A portion of the As-SBA-15 solid was calcined at 500 °C for 6 h under air with a temperature ramp of 1 °C/min and is denoted as SBA-r-500.

2.2. Preparation of the copper-based adsorbents

The adsorbents were prepared as follows: 1.52 g of copper acetylacetonate (Cu(acac)$_2$ from Sigma–Aldrich) was mixed with 4.5 g of As-SBA-15 in a flask that was then vigorously manually stirred for 1 min to homogenize the mixture. The resulting blue powder was then introduced in the crucibles of the grinding ball-mill (Philips Minimill) and was ball-milled for 30 min.

2.2.1. Cu/SBA-r-500

A first portion of the resulting ball-milled solid was calcined under air in a muffle furnace at 500 °C for 6 h with a ramp of 1 °C/min. Note that to get an homogenous sample after calcination, the powder was dispersed in the crucible so that to obtain a layer as thin as possible. The resulting material was green and is denoted as "Cu/SBA-r-500" where r designates the ramp calcination mode and 500 refers to the calcination temperature in °C.

2.2.2. Cu/SBA-f-500

A second portion of the ball-milled solid was flash-calcined: the muffle furnace was pre-heated at 500 °C and the sample was quickly introduced in and kept in it for 6 h at 500 °C. Note that this procedure was carried out with care since the sample ignited when introducing it in the furnace, due to the combustion of the Pluronic 123 surfactant. The resulting material was brown and is denoted as "Cu/SBA-f-500" where f designates the flash calcination mode.

2.2.3. Cu/SBA-r-700

The remaining portion of the sample was calcined under air in a muffle furnace at 700 °C for 6 h with a ramp of 1 °C/min. The resulting material was brown and denoted as "Cu/SBA-r-700".

2.3. Techniques of characterization

X-Ray powder diffraction (XRD) was performed in a reflection mode on a PANalytical X'Pert diffractometer (Cu Kα radiation, λ = 1.5418 Å) equipped with a X'Celerator detector. Measurements were achieved for 2θ angle values in the 3–70° range, by step of 0.02°, with a time of 220 s by step. The same diffractometer was used to record the XRD patterns at low angles (2θ range from 0.5 to 3°). In that case, a glass support was used as sample holder.

The XRD analysis of the aged material (after multicycle SO_x adsorption experiments) was performed on a STOE STADI-P diffractometer (Debye–Scherrer geometry) equipped with a curved germanium (1 1 1) primary monochromator and a linear position-sensitive detector (6° 2θ) using Cu Kα$_1$ radiation (λ = 1.5406 Å).

Transmission electron microscopy (TEM) micrographs were collected on a Philips CM200 microscope equipped with a LaB$_6$ filament. The accelerating voltage was 200 kV. Samples were previously dispersed in water and sonicated during 10 min. Then, five to ten drops of the solution were deposited onto Cu grids coated with a thin (5 nm thick) holey carbon support film.

Chemical analyses were performed using an X-Ray fluorescence (XRF) spectrometer (Philips MagiX). The samples were compacted in 13 mm diameter pellets.

Nitrogen physisorption was carried out on a Micromeritics Tristar apparatus. Prior to the measurements, the samples were outgassed at 150 °C for 15 h under vacuum. Specific surface areas, pore volumes and pore size distributions were determined by the BET and BJH methods, respectively.

Scanning electron microscopy (SEM) micrographs were obtained on a Philips XL 30 FEG microscope. Cu-X-ray mappings were obtained from the EDX analyzer Oxford Inca Si(Li) on the same microscope.

2.4. SO$_2$ chemisorption tests

The SO$_2$ chemisorption tests were performed in a fixed bed reactor. The adsorbents were previously pelletized (2 min at 0.25 ton/cm^2), crushed and sieved to retain the fraction having a particle diameter ranging from 225 to 450 μm. Samples were introduced in a vertical quartz reactor (6 mm inner diameter) fitted with a fused silica frit. The chemisorption experiments were performed at 400 °C, a temperature which corresponds to the conditions encountered in a gas turbine installations, using a gas mixture containing 250 ppm of SO$_2$ and 10 vol.% of O$_2$ diluted in nitrogen. The gas flow rate, equaling 13 NL/h, was adjusted by BROOKS 5850 mass flow controllers. The height of the adsorbent bed in the reactor was set at 2 cm in order to reach a gas hourly space velocity (GHSV) value of 25,000 h^{-1} which is representative of gas turbine exhaust conditions. The SO$_2$ outlet concentration was continuously measured by a UV absorption analyzer (Rosemount NGA 2000; range: 0–1000 ppm). The accuracy of the measurements, given by the manufacturer, is better than 1% of full scale. Before the SO$_2$ chemisorption step, the material was heated from 25 to 400 °C at a heating rate of 5 °C/min under pure N$_2$ and the temperature was maintained at 400 °C during 1 h. The dynamic SO$_2$ chemisorption capacity (C$_{ads}$ expressed in moles of adsorbed SO$_2$ per gram of adsorbent) is calculated by integrating the SO$_2$ breakthrough curve until the SO$_2$ concentration at the outlet of the reactor reaches 75 ppm. This value has been chosen since it is slightly lower than the SOx emission limit value currently enacted by the European regulation. The calculation is performed as follows:

$$C_{ads} = \frac{Q_g \int_{t_0}^{t_{75}} (C_0 - C) dt}{10^6 \times V_m \times m_{ads}}$$

where Q_g is the gas flow rate (in NL/h), C_0 and C are respectively the inlet (250 ppm) and outlet concentrations of SO$_2$ (in ppm), V_m is the molar volume (equaling 22.4 L at 0 °C and 1 atmosphere), m_{ads} is the mass of adsorbent (in gram) and t_0 and t_{75} (in hour) are respectively the starting time and the time at which the SO$_2$ concentration reaches 75 ppm.

2.5. Adsorbent regeneration by thermal decomposition of the sulfated adsorbents

The regeneration of the adsorbents after SO$_2$ chemisorption was performed in situ i.e., in the same experimental setup as the SO$_2$ chemisorption tests, under a nitrogen stream. The adsorbent was heated from 25 to 600 °C at 5 °C/min with a N$_2$ flow of 13 NL/h which corresponds to a GHSV value of 25,000 h^{-1}. This temperature of
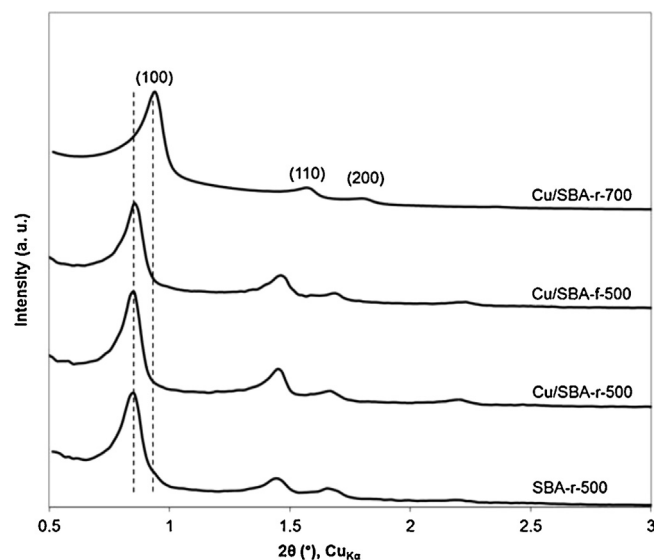

Fig. 1. Low angle XRD patterns of SBA-15 based materials. For a better visibility, the X-ray diffraction patterns are shifted along the *Y*-axis.

600 °C is sufficient to decompose copper sulfates as shown by previous thermogravimetric studies. The temperature was maintained at 600 °C until the SO$_2$ concentration at the outlet of the reactor dropped below 1 ppm, which corresponds to a duration of around 3 h at 600 °C. The SO$_2$ outlet concentration was continuously monitored by the UV absorption analyzer. The total SO$_2$ chemisorption capacity (TC$_{ads}$) of the material, expressed in moles of adsorbed SO$_2$ per gram of adsorbent) was calculated by integrating the SO$_2$ concentration curve over the duration of the TPD (Temperature Programmed Desorption), according to the following formula:

$$TC_{ads} = \frac{Q_g \int C dt}{10^6 \times V_m \times m_{ads}}$$

where Q_g is the gas flow rate (NL/h), C is the outlet concentration of SO$_2$ (in ppm), V_m is the molar volume (equaling 22.4 L at 0 °C and 1 atmosphere), m_{ads} is the mass of adsorbent (in gram).

3. Results and discussion

3.1. Characterization of the adsorbents

Table 1 summarizes the calcination procedure, chemical composition, color and textural properties of the SBA-15 mesoporous silica calcined at 500 °C (SBA-r-500) and of the three adsorbents. (Table 1) The Cu/SBA-r-500 sample is green, presumably due to the formation of Cu—O—Si species while the Cu/SBA-f-500 sample is brown due to the formation of small copper oxide particles, as discussed below. The same goes for the Cu/SBA-r-700 material which is brown presumably due to the formation of copper oxide resulting from copper species sintering at high temperature (700 °C). Note that the CuO loadings of the three adsorbents are lower than expected (CuO = 17.0 wt.%), due to a partial sublimation of Cu(acac)$_2$ during the calcination step [49]. This effect seems to be more pronounced for the Cu/SBA-f-500 sample (10.4 wt.% CuO versus 12.5 wt.% and 12.0 wt.% for the Cu/SBA-r-500 and Cu/SBA-r-700 samples, respectively). This may be due to the fact that during the ramp, copper acetylacetonate has the time to partially decompose into a less volatile copper compound (copper oxide).

The low angle XRD patterns shown in Fig. 1 confirm the presence of the P6mm hexagonal mesoporous structure of SBA-15 with XRD peaks assigned to (1 0 0), (1 1 0) and (2 0 0) reflection planes [50].

Table 1
Calcination procedure, chemical composition, color and textural properties of SBA-15 based materials.

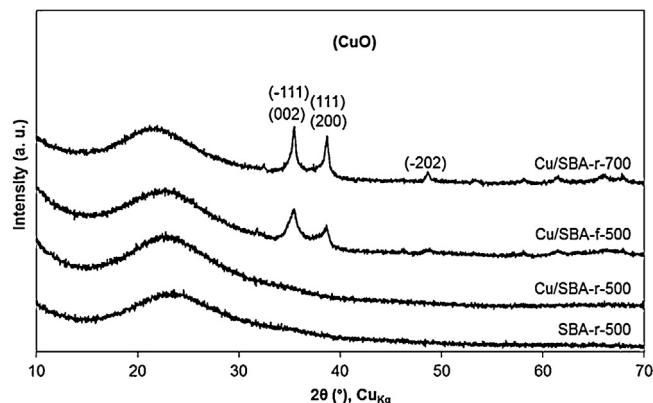| Sample	SBA-r-500	Cu/SBA-r-500	Cu/SBA-f-500	Cu/SBA-r-700
Calcination Conditions	Ramp 1 °C/min, 500 °C, 6 h	Ramp 1 °C/min, 500 °C, 6 h	Flash 500 °C, 6 h	Ramp 1 °C/min, 700 °C, 6 h
Color	White	Green	Brown	Brown
CuO content (wt.%)[a]	/	12.5	10.4	12.0
S_{BET} (m^2/g)	897	723	703	477
S_{BET} (m^2/g$_{SiO2}$)	897	826	784	542
Pore size (nm)	7.9	7.8	7.6	7.3
V_p (cm^3/g)	1.05	0.92	0.87	0.70
V_p (cm^3/g$_{SiO2}$)	1.05	1.05	0.97	0.79

[a] Based on XRF characterizations.
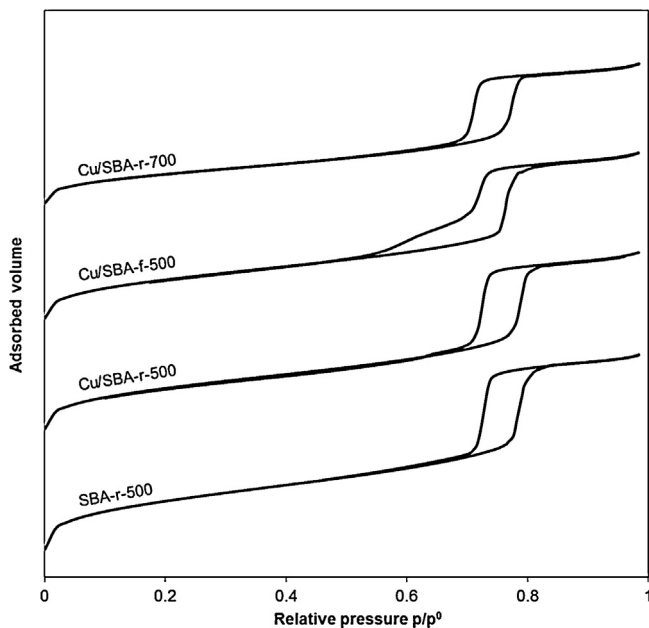
Fig. 2. Nitrogen adsorption-desorption isotherms of SBA-15 based materials. For a better visibility, the N$_2$ physisorption isotherms are shifted along the Y-axis.

Fig. 3. Wide angle XRD patterns of SBA-15 based materials. For a better visibility, the X-ray diffraction patterns are shifted along the Y-axis.

This means that for all samples, the mesoporous structure is preserved after the incorporation of copper. It must be emphasized that the diffraction peaks of the Cu/SBA-r-700 sample exhibit a slight shift towards higher angles which is characteristic of a smaller lattice parameter. This is attributed to the dehydroxylation reactions which occur at high temperature (700 °C), resulting in the contraction of the mesoporous network as reported in the literature [51,52].

Nitrogen physisorption isotherms of the adsorbents and the calcined SBA-15 material are reported in Fig. 2. The SBA-r-500 sample shows type IV adsorption–desorption isotherms with parallel adsorption and desorption branches and a well-defined hysteresis loop in the relative pressure range (p/p^0) of 0.7-0.8. According to the IUPAC classification, such isotherms correspond to OMSs with well-ordered cylindrical pores [53].

The adsorption and desorption isotherms of the Cu/SBA-r-500 material do not show significant modifications compared to those of the parent SBA-r-500 support, suggesting that the mesoporous structure is preserved after the incorporation of copper. This result is in agreement with the low angle XRD patterns (Fig. 1). As shown in Table 1, the Cu/SBA-r-500 sample exhibits a decrease of both its BET specific area (723 m^2/g) and porous volume (0.92 cm^3/g) as compared to the parent SBA-r-500 (897 m^2/g and 1.05 cm^3/g, respectively). Since these characteristics are expressed per gram of solid, these decreases might be ascribed to the densification of the mesoporous support due to the incorporation of copper and pos-

sibly to a slight alteration of the mesoporous structure during the grinding. The pore size distribution of the Cu/SBA-r-500 sample is similar (7.8 nm) to that of the parent SBA-r-500 (7.9 nm). The wide angle XRD pattern of the Cu/SBA-r-500 material does not show any CuO XRD peaks (Fig. 3), evidencing a high dispersion of copper or the presence of amorphous copper species.

Indeed, according to the literature, copper might be in strong interaction with the support as Cu—O—Si species which could explain both the green color of the sample and the absence of diffraction peaks [20,44,45,54–57]. This result is supported by the Cu-X-ray mapping (Fig. 4 B) which shows a homogeneous distribution of copper on the support at the micrometric scale.

Actually, TEM micrographs A and B of Fig. 5 highlight the absence of particles although EDX analysis (not reported) confirms the presence of elemental copper.

On the contrary, the Cu/SBA-f-500 sample contains visible CuO nanoparticles. Indeed, typical diffraction peaks (−1 1 1, 0 0 2, 1 1 1, 2 0 0 and −2 0 2) of crystalline CuO are observed on the Cu/SBA-f-500 XRD pattern shown in Fig. 3. Their broad shape suggests a small average crystallite size. This is confirmed by the TEM micrographs C and D of Fig. 5, in which CuO particles with a size ranging from 5 nm to 10 nm are observed. According to the micrograph D, it is likely that most of the small particles are located inside the porous network. Additionally, the particle size is close to the pore diameter which suggests that their growth is limited by a confinement effect. However, as observed on the TEM micrograph C (Fig. 5) and the Cu-X-Ray mapping (Fig. 4D, see arrows), some larger CuO particles (100–200 nm) are also present outside the channels. The desorption branch of the N$_2$ isotherms (Fig. 2) exhibits a delay in the relative pressure range of p/p^0 = 0.5–0.7, while the adsorption branch does not show any significant change as compared to the one of the parent SBA-r-500 material. This behavior is characteristic of a partial blocking of the pores resulting from the presence of CuO particles in the mesoporous network. The specific BET surface area
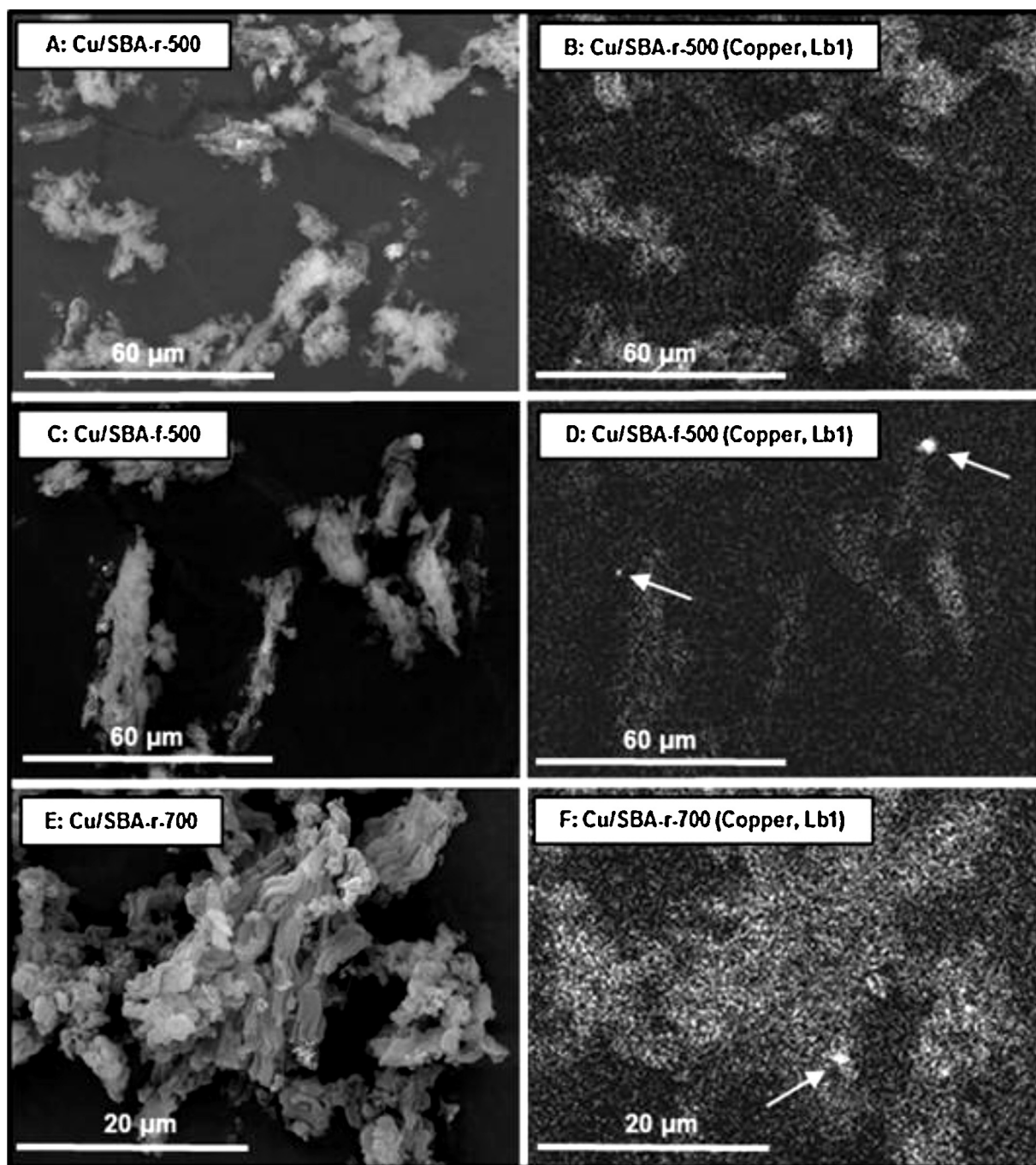
Fig. 4. SEM micrographs (A, C and E) and corresponding Cu-X-ray mappings (B, D and F) of SBA-15 based materials.

(703 m^2/g), porous volume (0.87 cm^3/g) and pore size (7.6 nm) are slightly lower than those of the Cu/SBA-r-500 sample (723 m^2/g, 0.92 cm^3/g and 7.8 nm, respectively). This is probably associated with the presence of the small copper oxide particles rather than to the Cu—O—Si species.

As a partial interesting conclusion, the significant differences between the adsorbents prepared from ramp and flash calcinations in term of copper dispersion reflect the strong influence of the calcination method (ramp vs flash calcination) since the flash calcination induces the formation of CuO nanoparticles while the ramp calcination favors the formation of highly dispersed copper-based species in strong interaction with the support (Cu—O—Si).

As expected [51,52] due to the higher calcination temperature, the specific BET surface area of the Cu/SBA-r-700 sample (477 m^2/g) is significantly lower than that of the Cu/SBA-r-500 adsorbent (723 m^2/g). As discussed above, a higher calcination temperature leads to the contraction of the mesoporous network resulting in smaller pore size and volume (7.3 nm and 0.70 cm^3/g), which is in agreement with the smaller lattice parameter deduced from low angle XRD patterns (Fig. 1). The calcination at 700 °C also results in copper species sintering since both the smaller (5-10 nm) and bigger (a few μm) particles are now visible by TEM (Fig. 5, micrographs E and F) and SEM (Fig. 4F, see arrow) analyses. It remains difficult to determine from the TEM and SEM images the relative proportions of small or big CuO particles. However the sharpness
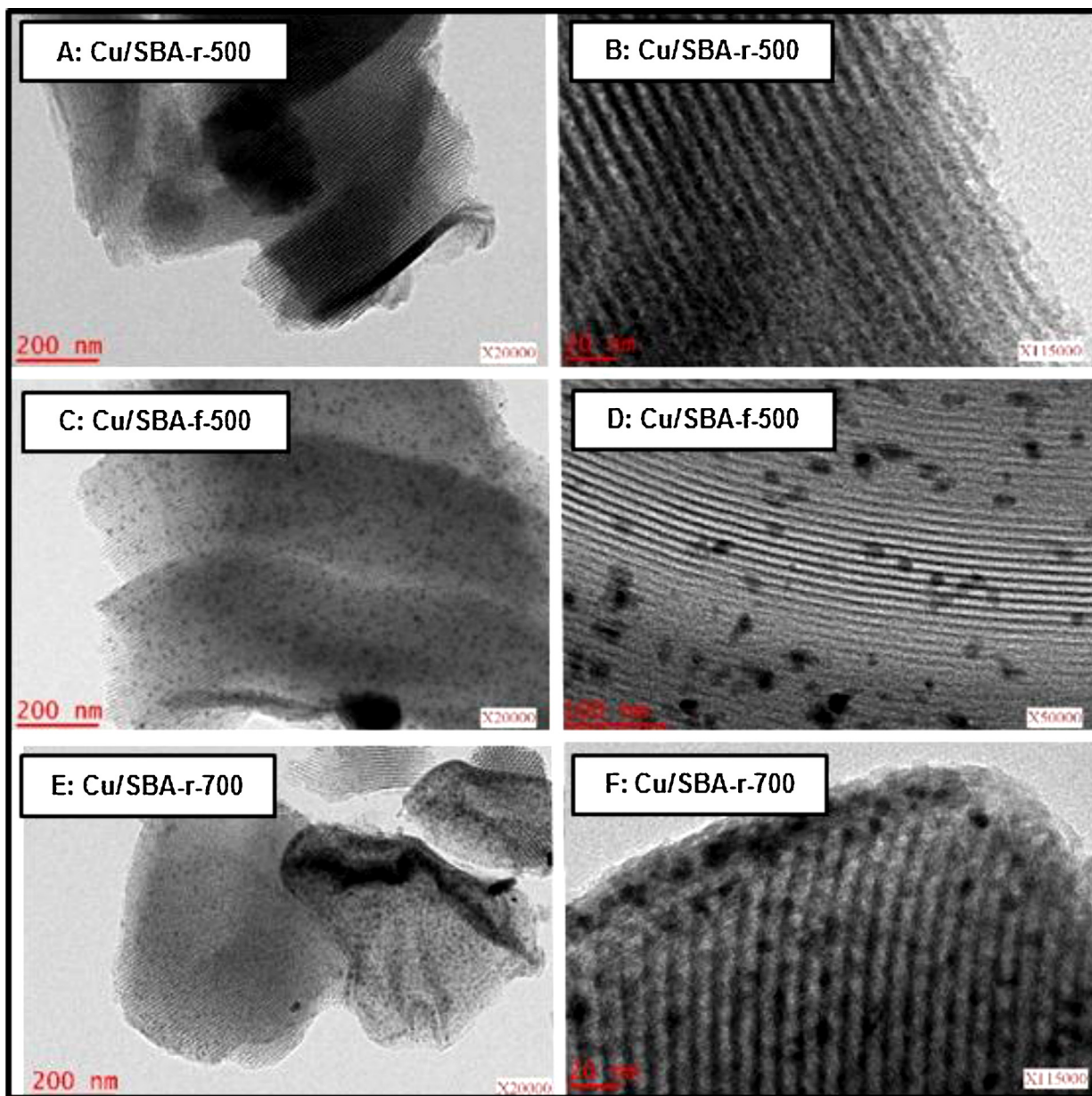
Fig. 5. TEM micrographs of the different SBA-15 based adsorbents. A and B: Cu/SBA-r-500, C and D: Cu/SBA-f-500, E and F: Cu/SBA-r-700.

of the XRD peaks (Fig. 3), unambiguously shows that the average crystallite size of the Cu/SBA-r-700 sample is higher than that of the Cu/SBA-f-500 material.

3.2. SO$_2$ chemisorption tests

The SO$_2$ adsorption testing of the three adsorbents was performed in a fixed bed reactor. The SO$_2$ breakthrough curves are reported in Fig. 6. The SO$_2$ chemisorption capacities expressed in mol$_{SO2}$/g$_{ads}$ are reported in Table 2. Given that copper is present under various states (Cu—O—Si species, small CuO particles and large CuO particles) in the adsorbents, we aimed to evaluate the DeSO$_X$ efficiency of these different copper species. Thus, the sulfation ratio of copper was introduced (Table 2) as a representative value of the DeSO$_x$ efficiency of the active phase (copper) incorporated in the SBA-15 support.

At the saturation of the three adsorbents, the SO$_2$ concentration measured at the outlet of the reactor varies from 180 ppm to
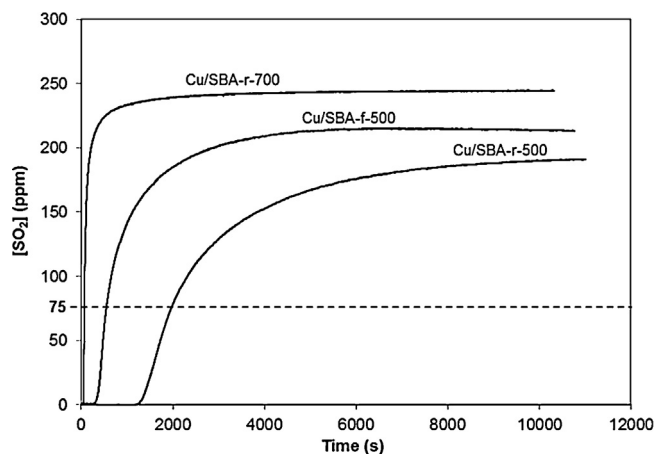

Fig. 6. SO$_2$ breakthrough curves of SBA-15 based adsorbents.

Table 2
CuO loading, SO_2 dynamic chemisorption capacities and copper sulfation ratios of SBA-15 based adsorbents.

Sample	Cu/SBA-r-500	Cu/SBA-f-500	Cu/SBA-r-700
CuO (mol/g_{ads})	1.6×10^{-3}	1.3×10^{-3}	1.5×10^{-3}
C_{ads} at 75 ppm[a] (mol$_{SO2}$/g_{ads})	4.5×10^{-4}	1.3×10^{-4}	1.7×10^{-5}
Copper sulfation ratio at 75 ppm (%)[b]	28.1	10.0	1.1

[a] Determined by integration of the SO_2 breakthrough curves.

[b] Correspond to C_{ads} at 75 ppm $\times$ 100/CuO loading.

240 ppm whereas that of injected SO_2 is 250 ppm. This suggests that a fraction of the injected SO_2 is still oxidized by the adsorbent, yielding SO_3 which is not detected by the UV analyzer. The SO_2 oxidation activity at saturation is related to the copper dispersion in the materials, and follows the trend: Cu/SBA-r-500 » Cu/SBA-f-500 > Cu/SBA-r-700. The higher the copper dispersion, the greater the oxidation activity of the adsorbent at saturation.

The Cu/SBA-r-700 sample appears as the least efficient adsorbent since the breakthrough occurs at only 68 s which corresponds to a dynamic SO_2 chemisorption capacity of $C_{ads} = 1.7 \times 10^{-5}$ mol$_{SO2}$/g_{ads} ("dynamic" meaning calculated at $[SO_2]_{outlet} = 75$ ppm). In other words, only 1.1% of the CuO is sulfated when the $[SO_2]_{outlet}$ reaches 75 ppm. Such a poor efficiency is tied with the presence of large CuO particles in this material. As expected and according to the literature [4,6], one can conclude that the sulfation of the bulk CuO particles is a very slow and limiting process, especially in the case of large particles. Centi et al. suggested that during the DeSO$_x$ reaction, there is a rapid formation of superficial sulfate species, which, because of the higher cell volume of CuSO$_4$ compared to CuO, CuSO$_4$ entirely covers the latter, and slows down the formation of further subsurface sulfate species [4].

The Cu/SBA-f-500 adsorbent is more efficient than the Cu/SBA-r-700 sample as its breakthrough occurs at around 300 s. This adsorbent exhibits a dynamic sulfation rate of 10.0% and an SO_2 uptake capacity of $C_{ads} = 1.3 \times 10^{-4}$ mol$_{SO2}$/g_{ads}. This higher efficiency reflects the better dispersion of copper oxide as shown by the characterization results set out above.

The most efficient adsorbent is by far the Cu/SBA-r-500 sample which exhibits an SO_2 uptake capacity of $C_{ads} = 4.5 \times 10^{-4}$ mol$_{SO2}$/g_{ads} and a copper sulfation rate of 28.1%. This high efficiency reflects the high dispersion of the copper species. Moreover, it is likely that the diffusion of gaseous species in this sample is faster than for the Cu/SBA-f-500 sample. Indeed, the presence of CuO particles in the channels of the Cu/SBA-f-500 material probably entails diffusional limitations as suggested by the N_2 desorption isotherm profile.

Therefore, like the SO_2 oxidation activity, the copper sulfation rate appears to be correlated with the dispersion of copper. The higher the copper dispersion, the greater the SO_2 adsorption capacity, in agreement with the findings of Centi et al. [4].

3.3. Regeneration tests of the Cu/SBA-r-500 adsorbent

Since the Cu/SBA-r-500 adsorbent boasts the best SO_2 adsorption efficiency, it was decided to investigate its behavior through multicycle experiments in order to evaluate its potential as a regenerable adsorbent. The material was subjected to 7 successive chemisorption-regeneration cycles. As reported in the experimental section, the regeneration was performed by thermal decomposition at 600 °C of the copper sulfate under a N_2 flow (TPD). The SO_2 breakthrough curves performed on the Cu/SBA-r-500 adsorbent during cycling experiment are shown in Fig. 7.

It is very interesting though unexpected to see that the efficiency of the Cu/SBA-r-500 adsorbent strongly increases between the first and the second cycle (chemisorption 1 + TPD 1). It must be
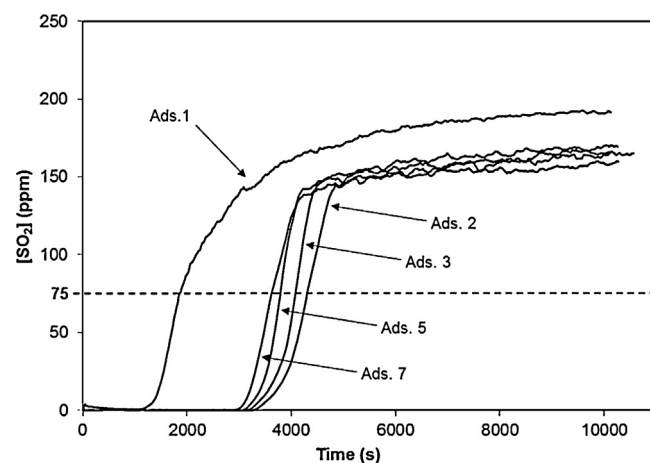
Fig. 7. SO_2 breakthrough curves of the Cu/SBA-r-500 adsorbent submitted to multicycle operations.

emphasized that the shape of the first SO_2 breakthrough curve is different from the following ones and the SO_2 oxidation activity at saturation (around 10,000 s) is lower than for the following cycles ($[SO_2]_{outlet} = 193$ ppm instead of 170–180 ppm). This suggests some evolution of the SO_2 oxidation-chemisorption properties of the material over the cycles, especially between the first one and the second one. As shown in Table 3, the dynamic copper sulfation ratio is of 27.0% for the first SO_2 chemisorption cycle and remarkably increases up to 64.4% for the second cycle. Then, it slowly decreases in the next cycles, reaching 53.9% for the seventh one.

As discussed below, this slight decrease of the adsorbent efficiency is attributed to a CuO sintering effect. Thus, it seems that the first SO_2 chemisorption run followed by a regeneration at 600 °C under nitrogen leads to a more active adsorbent. In order to determine which from the chemisorption step or the thermal treatment (i.e., the TPD) step is at the origin of this effect, the fresh Cu/SBA-r-500 adsorbent was subjected to a thermal treatment at 600 °C under N_2 flow, before sulfation. The SO_2 breakthrough curves of the treated and non-treated adsorbents are shown in Fig. 8.

Interestingly, the sample displays after this treatment a SO_2 breakthrough curve similar in shape and duration to those of the cycles 2–7 of the Cu/SBA-r-500 adsorbent (Fig. 7). The dynamic chemisorption capacity during this first cycle reaches 9.0×10^{-4} mol$_{SO2}$/g_{ads} corresponding to a copper sulfation ratio of 56.2%. This result shows that the thermal treatment at 600 °C under nitrogen is actually responsible for the activity enhancement of the Cu/SBA-r-500 sample between the first and second cycle (Fig. 8). It is noteworthy that the characterization (N_2 physisorption, XRD, SEM and TEM, not reported) of the Cu/SBA-r-500 sample after treatment at 600 °C does not show significant differences as compared to the non-treated material. More especially, no CuO particles are observed by TEM, suggesting that there is no copper sintering during the thermal treatment.

According to the literature, it is possible that such a thermal treatment under nitrogen results in the reduction of the Cu^{2+} copper species to Cu^+ species [58,59] which might be more active for

Table 3
Dynamic and total SO_2 chemisorption capacities of the Cu/SBA-r-500 adsorbent submitted to multicycle operations.

| Cycle	1	2	3	4	5	6	7
C_{ads} at 75 ppm[a] (mol_{SO2}/g_{ads})	4.3×10^{-4}	10×10^{-4}	9.7×10^{-4}	/	9.1×10^{-4}	8.7×10^{-4}	8.6×10^{-4}
Dynamic copper sulfation ratio at 75 ppm (%)[b]	27.0	64.4	60.8	/	56.7	54.4	53.9
TC_{ads} at saturation (mol_{SO2}/g_{ads})[c]	/	7.1×10^{-4}	6.5×10^{-4}	/	8.9×10^{-4}	6.8×10^{-4}	7.5×10^{-4}

[a] Determined by integration of the SO_2 breakthrough curves.
[b] Correspond to C_{ads} at 75 ppm × 100/CuO loading.
[c] Determined by integration of the TPD curves.
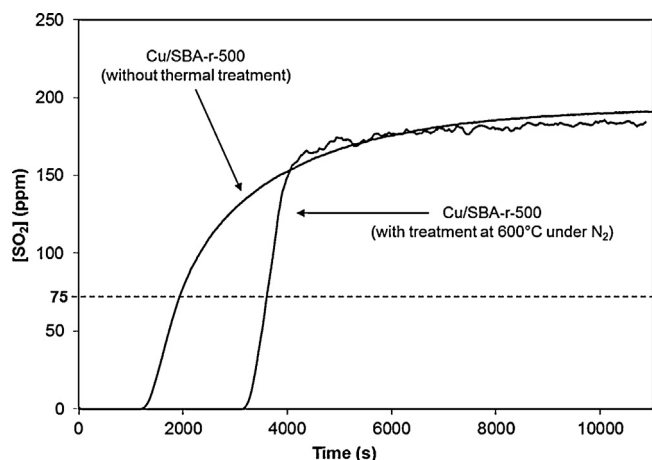
Fig. 8. SO_2 breakthrough curves of the Cu/SBA-r-500 adsorbent with and without the thermal treatment at 600 °C.
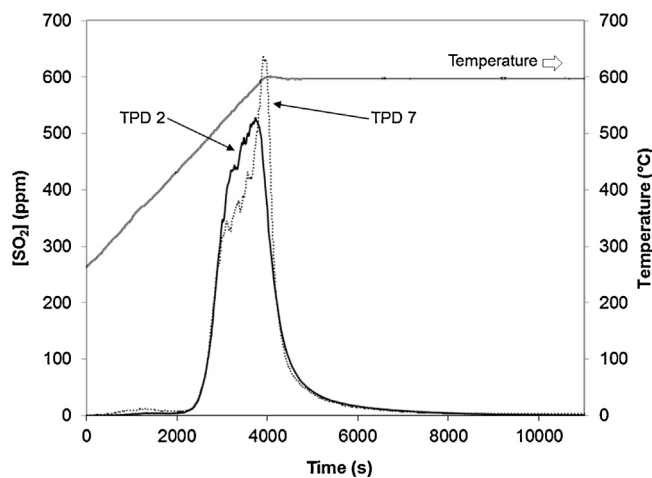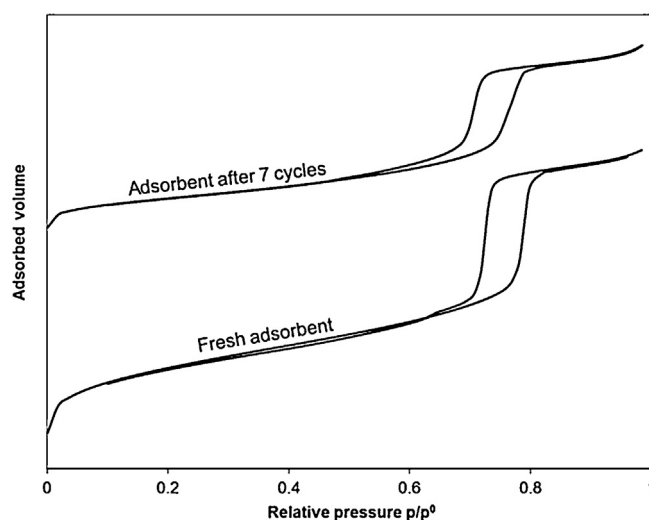

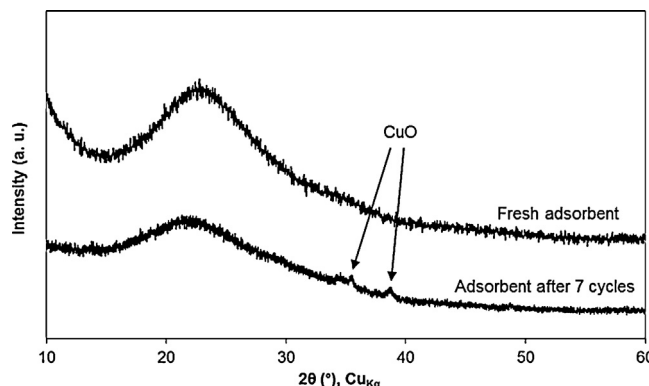**Fig. 9.** TPD curves (cycles 2 and 7) of the Cu/SBA-r-500 adsorbent.

Fig. 10. N_2 physisorption isotherms of the Cu/SBA-r-500 adsorbent before and after 7 sulfation-regeneration cycles. For a better visibility, the isotherms are shifted along the Y-axis.

Fig. 11. Wide angle XRD patterns of the fresh Cu/SBA-r-500 adsorbent and the same material after 7 sulfation-regeneration cycles. For a better visibility, the X-ray diffraction patterns are shifted along the Y-axis.

the oxidation-chemisorption of SO_2. This phenomenon is currently under investigation.

The TPD curves obtained during the successive regeneration steps are shown in Fig. 9. For the sake of concision, only the curves of the second and seventh regeneration cycles are given.

One clearly observes over the successive cycles a shift of the process of decomposition of the sulfated copper towards higher temperatures. This shift reflects the formation of sulfated copper species that are more difficult to decompose. It is likely that these species are bulk-like $CuSO_4$ species formed by the sulfation of larger CuO particles which result from the coalescence by sintering of the initial copper species, as discussed below. The total SO_2 chemisorption capacity data determined by integration of the TPD curves

are reported in Table 3. Note that these values are obtained after the saturation of the adsorbent (the adsorption runs are continued up to 10,000 s as shown in Fig. 7) and should thus correspond to the total chemisorption capacity of the adsorbent. Surprisingly, the total SO_2 uptake capacities obtained by TPD are lower than the corresponding dynamic ones calculated from the SO_2 breakthrough curves integration until $[SO_2]_{outlet} = 75$ ppm. This result is believed to come from the formation of both SO_2 and SO_3 (thermodynamic equilibrium) during the thermal decomposition of $CuSO_4$. As mentioned above, SO_3 is not detected by the UV analyzer. Thus
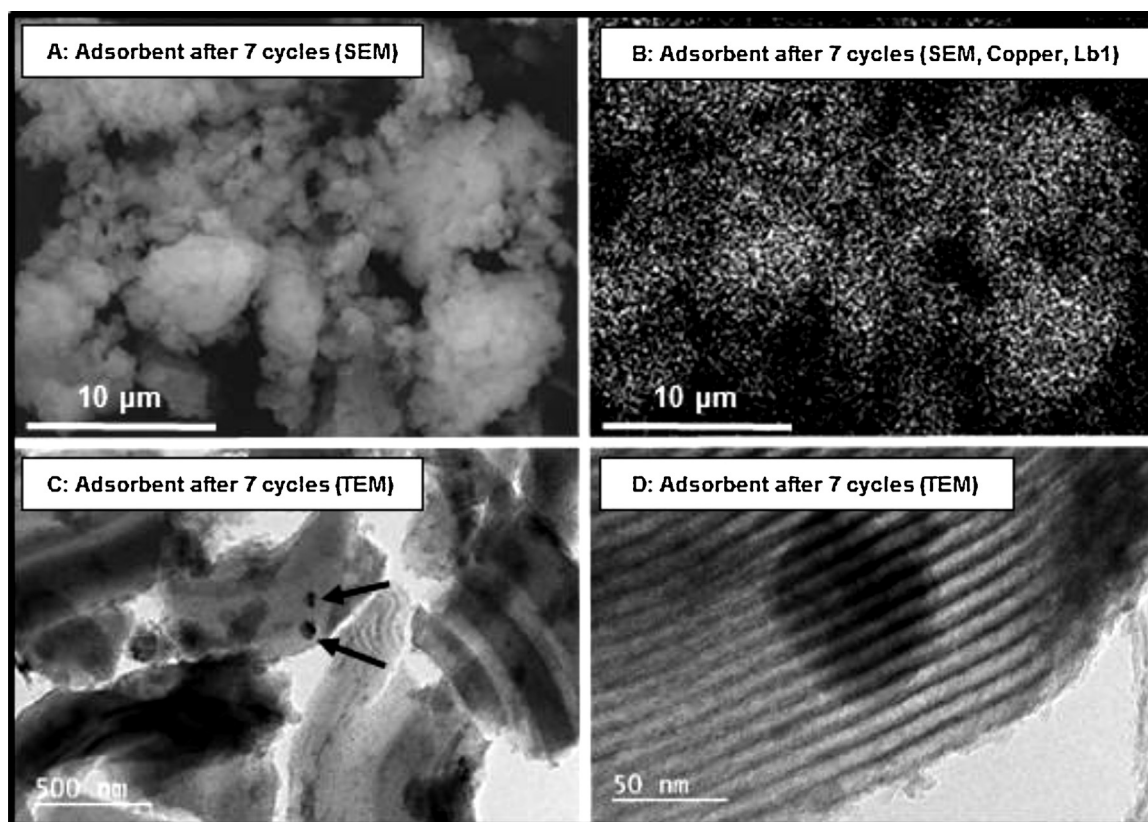
Fig. 12. SEM micrograph (A), corresponding Cu-X-ray mappings (B) and TEM micrographs (C and D) of the Cu/SBA-r-500 adsorbent after 7 sulfation-regeneration cycles.

the values obtained by TPD are not representative of the real total SO_2 uptake capacities of the adsorbent.

3.4. Characterization of the Cu/SBA-r-500 adsorbent after 7 operation cycles

The Cu/SBA-r-500 adsorbent was characterized after 7 sulfation-regeneration cycles. The nitrogen physisorption isotherms of the fresh and aged material are reported in Fig. 10. For the aged sample, the capillary condensation starts at a lower relative pressure and is less steep, revealing a widening of the pore size distribution toward smaller pore size. The porous volume ($0.54\,cm^3/g$) and BET surface area ($312\,m^2/g$) are lower than those of the fresh material ($0.92\,cm^3/g$ and $723\,m^2/g$, respectively). These results show that the mesoporous structure has been altered along the 7 cycles. The CuO sintering process is correlated with this alteration. In fact this effect is closely related to the metal loading and the textural properties of the support [60,61].

The sintering is clearly evidenced on the XRD pattern of the aged Cu/SBA-r-500 adsorbent which exhibits small CuO peaks while the fresh material shows none of them (Fig. 11).

Note that the XRD analysis of the fresh adsorbent was performed on a plate sample holder, while the one of the aged material was carried out in a capillary tube. This explains the difference in signal intensities of the amorphous SiO_2 (broad peak over the range of 2 from 15 to 30°). The SEM micrograph and the corresponding Cu-X-ray mapping of the aged sample are shown in Fig. 12.

They show a homogeneous distribution of copper on the support and the absence of any CuO particles of a few μm size. However the TEM micrographs visible in the same figure, show small CuO particles (black arrows) with a size ranging from 50 nm to 100 nm and which seem to be located outside the porous structure. These

nascent CuO particles are reflected by the CuO XRD peaks and are assumed to be responsible of the slight adsorbent deactivation.

In summary, the Cu/SBA-r-500 adsorbent exhibits the best $DeSO_X$ efficiency which correlates with its high degree of dispersion of copper. However, this adsorbent undergoes a slight, progressive deactivation which is attributed to a copper species sintering process that develops progressively over the successive chemisorption-regeneration cycles. However, the weak intensity of the XRD peaks after 7 cycles suggests that this copper species sintering stays a minor one, probably thanks to the high specific surface area of the mesoporous silica SBA-15 support that maintains the active copper centers distant enough from each other [61]. This allows the adsorbent to retain a significant efficiency after multiple cycles.

4. Conclusion

Three adsorbents featuring different copper oxide dispersions were synthesized through solid state grinding of a copper precursor consisting in copper acetylacetonate in mixture with some as-synthesized SBA-15 taken as a mesoporous silica support. The mesoporous structure appears to be well preserved after the copper incorporation. A flash calcination at 500 °C leads to the formation of CuO particles that are very small (5–10 nm) and located in the channels of the SBA-15 mesoporous silica but these small particles are accompanied by some larger ones. On the contrary, a ramp calcination at 500 °C results in the formation of only highly dispersed copper species that are in strong interaction with the support and are invisible by TEM and SEM. However the use of a higher ramp calcination temperature (700 °C) entails a significant sintering effect of copper. As expected, the $DeSO_X$ efficiency of the adsorbents was found to increase with the degree of copper dispersion. Cyclic adsorption/regeneration runs performed on the

most efficient adsorbent (Cu/SBA-r-500 sample) showed an unexpected increase in the SO_2 uptake capacity between the first and second cycle. It was experimentally verified that the thermal treatment at 600 °C under a flow of nitrogen which is used to regenerate the adsorbent, causes this performance improvement. As a possible explanation, there might be some reduction of Cu^{2+} ions to Cu^+ ions which could be more efficient than Cu^{2+} for the chemisorption of SO_2. Accordingly a jump from 27% (ca 1/4) to 64% (ca 2/3) of the dynamic copper sulfation ratio was observed from the first to the second cycle. A progressive but slight decrease of the adsorbent efficiency was observed along the chemisorption-regeneration cycles. According to the complete set of characterizations performed during this work on the adsorbent having passed seven cycles, this decay is also attributable to a CuO sintering effect. Finally, it must be stressed that in spite of the challenging GHSV value used in this work, which corresponds to a short contact time of 0.15 s, we have measured relatively high dynamic copper sulfation ratios, which emphasizes the high DeSO$_X$ performances of highly dispersed copper species.

Acknowledgments

References

[1] A.P. Tsimpidi, V.A. Karydis, Spyros N. Pandis, J. Air Waste Manage. Assoc. 57 (2007) 1489–1498.
[2] Y. Mathieu, L. Tzanis, M. Soulard, J. Patarin, M. Vierling, M. Moliere, Fuel Process. Technol. 114 (2013) 81–100.
[3] G. Centi, S. Perathoner, Dev. Chem. Ens. Mineral Process. 8 (2000) 441–463.
[4] G. Centi, N. Passarini, S. Perathoner, A. Riva, Ind. Eng. Chem. Res. 31 (1992) 1947–1955.
[5] S.S. Pollack, W.P. Chisholm, R.T. Obermyer, S.W. Hedges, M. Ramanathan, P.A. Montano, Ind. Eng. Chem. Res. 27 (1988) 2276–2282.
[6] K.S. Yoo, S.D. Kim, S.B. Park, Ind. Eng. Chem. Res. 33 (1994) 1786–1791.
[7] H. Dathe, P. Haider, A. Jentys, J.A. Lercher, J. Phys. Chem. B 110 (2006) 10729–10737.
[8] H. Dathe, P. Haider, A. Jentys, J.A. Lercher, J. Phys. Chem. B 110 (2006) 26024–26032.
[9] C. Macken, B.K. Hodnett, Ind. Eng. Chem. Res. 39 (2000) 3868–3874.
[10] M. Waqif, O. Saur, J.C. Lavalley, S. Perathoner, G. Centi, J. Phys. Chem. 95 (1991) 4051–4058.
[11] J.H.A. Kiel, W. Prins, W.P.M. Van Swaaij, Appl. Catal. B Environ. 1 (1992) 13–39.
[12] A. Corma, Chem. Rev. 97 (1997) 2373–2419.
[13] A. Taguchi, F. Schüth, Microporous Mesoporous Mater. 77 (2005) 1–45.
[14] J.P. Gabaldon, M. Bore, A.K. Datye, Top. Catal. 44 (2007) 253–262.
[15] X. Zhong, J. Barbier Jr., D. Duprez, H. Zhang, S. Royer, Appl. Catal. B Environ. 121–122 (2012) 123–134.
[16] A. Ungureanu, B. Dragoi, A. Chirieac, S. Royer, D. Duprez, E. Dumitriu, J. Mater. Chem. 21 (2011) 12529–12541.
[17] L.-F. Chen, P.-J. Guo, L.-J. Zhu, M.-H. Qiao, Appl. Cata. A Gen. 356 (2009) 129–136.
[18] X. Guo, A. Yin, W.-L. Dai, K. Fan, Catal. Lett. 132 (2009) 22–27.
[19] N. Brodie-Linder, R. Besse, F. Audonnet, S. Lecaer, J. Deschamps, Microporous Mesoporous Mater. 132 (2010) 518–525.
[20] Y.M. Wang, Z.Y. Wu, J.H. Zhu, J. Solid State Chem. 177 (2004) 3815–3823.
[21] A. Ungureanu, B. Dragoi, A. Chirieac, C. Ciotonea, S. Royer, D. Duprez, A.S. Mamede, M. Dumitriu, ACS Appl. Mater. Interfaces 5 (2013) 3010–3025.
[22] B. Dragoi, A. Ungureanu, A. Chirieac, V. Hulea, S. Royer, E. Dumitriu, Catal. Sci. Technol. 3 (2013) 2319–2329.
[23] C. Ciotonea, B. Dragoi, A. Ungureanu, A. Chirieac, S. Petit, S. Royer, E. Dumitriu, Chem. Commun. 49 (2013) 7665–7667.
[24] S.L. Soled, E. Iglesia, R.A. Fiato, J.E. Baumgartner, H. Vroman, S. Miseo, Top. Catal. 26 (2003) 101–109.
[25] P. Maki-Arvela, D.Y. Murzin, Appl. Cata. A Gen. 451 (2013) 251–281.
[26] F. Negrier, E. Marceau, M. Che, J.-M. Giraudon, L. Gengembre, A. Löfberg, J. Phys. Chem. B 109 (2005) 2836–2845.
[27] S.-S. Lee, H.-I. Park, B.-K. Park, S.-H. Byeon, Mater. Sci. Eng. B 135 (2006) 20–24.
[28] M. Che, Z.X. Cheng, C. Louis, J. Am. Chem. Soc. 117 (1995) 2008–2018.
[29] T. Toupance, M. Kermarec, C. Louis, J. Phys. Chem. B 104 (2000) 965–972.
[30] J.R.A. Sietsma, J.D. Meeldijk, J.P. den Breejen, M. Versluijs-Helder, A. Jos van Dillen, P.E. de Jongh, K.P. de Jong, Angew. Chem. Int. Ed. 46 (2007) 4547–4549.
[31] J. van de Loosdrecht, S. Barradas, E.A. Caricato, N.G. Ngwenya, P.S. Nkwanyana, M.A.S. Rawat, B.H. Sigwebela, P.J. van Berge, J.L. Visagie, Top. Catal. 26 (2003) 121–127.
[32] P. Munnik, M. Wolters, A. Gabrielsson, S.D. Pollington, G. Headdock, J.H. Bitter, P.E. de Jongh, K.P. de Jong, J. Phys. Chem. C 115 (2011) 14698–14706.
[33] J.R.A. Sietsma, H. Friedrich, A. Broersma, M. Versluijs-Helder, A.J. van Dillen, P.E. de Jongh, K.P. de Jong, J. Catal. 260 (2008) 227–235.
[34] K.P. De Jong, P.E. De Jongh, J.R.A. Sietsma, A.J. Van Dillen, (2009), Patent EP2061595.
[35] A. Hahn, T. Ressler, R.E. Jentoft, F.C. Jentoft, Chem. Commun. (2001) 537–538.
[36] J.R.A. Sietsma, J.D. Meeldijk, M. Versluijs-Helder, A. Broersma, A.J. Van Dillen, P.E. de Jongh, K.P. de Jong, Chem. Mater. 20 (2008) 2921–2931.
[37] B. Vos, E. Poels, A. Bliek, J. Catal. 198 (2001) 77–88.
[38] M. Wolters, L.J.W. Van Grotel, T.M. Eggenhuisen, J.R.A. Sietsma, K.P. De Jong, P.E. de Jongh, Catal. Today 163 (2011) 27–32.
[39] X. Sun, Y. Shi, P. Zhang, C. Zheng, X. Zheng, F. Zhang, Y. Zhang, N. Guan, D. Zhao, G.D. Stucky, J. Am. Chem. Soc. 133 (2011) 14542–14545.
[40] L. Vradman, M.V. Landau, D. Kantorovich, Y. Koltypin, A. Gedanken, Microporous Mesoporous Mater. 79 (2005) 307–318.
[41] A.H. Janssen, C.-M. Yang, Y. Wang, F. Schüth, A.J. Koster, K.P. de Jong, J. Phys. Chem. B 107 (2003) 10552–10556.
[42] Y.M. Wang, Z.Y. Wu, L.Y. Shi, J.H. Zhu, Adv. Mater. 17 (2005) 323–327.
[43] Q. Jiang, Z.Y. Wu, Y.M. Wang, Y. Cao, C.F. Zhou, J. Hua Zhu, J. Mater. Chem. 16 (2006) 1536–1542.
[44] X.-C. Shao, L.-H. Duan, Y.-Y. Wu, X.-C. Qin, W.-G. Yu, Y. Wang, H.-L. Li, Z.-L. Sun, L.-J. Song, Acta Phys. Chim. Sin. 28 (2012) 1467–1473.
[45] C.F. Zhou, Y.M. Wang, Y. Cao, T.T. Zhuang, W. Huang, Y. Chun, J.H. Zhu, J. Mater. Chem. 16 (2006) 1520–1528.
[46] Y.M. Wang, Z.Y. Wu, H.J. Wang, J.H. Zhu, Adv. Funct. Mater. 16 (2006) 2374–2386.
[47] W.-H. Tian, L.-B. Sun, X.-L. Song, X.-Q. Liu, Y. Yin, G.-S. He, Langmuir 26 (2010) 17398–17404.
[48] Y. Yin, W.-J. Jiang, X.-Q. Liu, Y.-H. Li, L.-B. Sun, J. Mater. Chem. 22 (2012) 18514–18521.
[49] R. Teghil, D. Ferro, L. Bencivenni, M. Pelino, Thermochim. Acta 44 (1981) 213–222.
[50] D. Zhao, J. Feng, Q. Huo, N. Melosh, G.H. Fredrickson, B.F. Chmelka, G.D. Stucky, Science 279 (1998) 548–552.
[51] F. Bérubé, S. Kaliaguine, Microporous Mesoporous Mater. 115 (2008) 469–479.
[52] T. Benamor, L. Michelin, B. Lebeau, C. Marichal, Microporous Mesoporous Mater. 147 (2012) 334–342.
[53] F. Rouquerol, J. Rouquerol, K. Sing, Adsorption by Powders and Porous Solids, Academic Press (Elsevier), San Diego, 1999.
[54] S.J. Gentry, P.T. Walsh, J. Chem. Soc. Faraday. Trans. 1 (78) (1982) 1515–1523.
[55] C. Huo, J. Ouyang, Sci. Rep. 4 (2013) 3682.
[56] Y. Kong, H. Zhu, G. Yang, X. Guo, W. Hou, Q. Yan, M. Gu, C. Hu, Adv. Funct. Mater. 14 (2004) 816–820.
[57] G.C. Bond, S.N. Namijo, J.S. Wakeman, J. Mol. Catal. 64 (1991) 305–319.
[58] M. Popova, A. Ristic, M. Mazaj, D. Maucec, M. Dimitrov, N. Novak Tusar, ChemCatChem 6 (2014) 271–277.
[59] S.C. Larsen, A. Aylor, A.T. Bell, J.A. Reimer, J. Phys. Chem. 980 (1994) 11533–11540.
[60] G. Prieto, M. Shakeri, K.P. de Jong, P.E. de Jongh, ACS Nano 8 (2014) 2522–2531.
[61] G. Prieto, J. Zečević, H. Friedrich, K.P. de Jong, P.E. de Jongh, Nat. Mater. 12 (2013) 34–39.